

Article

Process–Structure–Property Correlations in Twin-Screw Extrusion of Graphitic Negative Electrode Pastes for Lithium Ion Batteries Focusing on Kneading Concentrations

Kristina Borzutzki ^{1,*}, Markus Börner ², Olga Fromm ², Uta Rodehorst ² and Martin Winter ^{2,3}

¹ Fraunhofer Research Institution for Battery Cell Production FFB, 48165 Münster, Germany

² MEET Battery Research Center, University of Münster, Corrensstrasse 46, 48149 Münster, Germany; markus.boerner@uni-muenster.de (M.B.)

³ Helmholtz-Institute Münster (HI MS), Forschungszentrum Jülich GmbH, Corrensstrasse 46, 48149 Münster, Germany

* Correspondence: kristina.borzutzki@ffb.fraunhofer.de

Abstract

A continuous mixing process with a twin-screw extruder was investigated for graphite-based negative electrode pastes for high-power applications. In the extrusion-based mixing process, the first kneading concentration is one of the key processing parameters for systematic optimization of relevant electrode paste properties like viscosity and particle size distribution. For different active materials at a constant electrode paste composition, a clear correlation of increasing kneading concentration with decreasing viscosity can be observed up to a certain reversal point, initiating a change in the trend and the rheological behavior, thus indicating a process limit. The fundamental effects causing this change and the associated impact on materials and battery performance were evaluated by applying further analytical methods and electrochemical characterization. It is revealed that the change in viscosity is associated with enhanced de-agglomeration of the carbon black additive and with partial particle grinding of the active material and thus a partial change in the interlayer distance of graphene layers and, correspondingly, the electrochemical behavior of the active material. Beyond this, correlations between processing parameters and product properties are presented. Furthermore, indicators are suggested with which monitoring of the machine parameters enables the detection of changes in the electrode paste characteristics.



Academic Editor: Teofilo Rojo

Received: 28 May 2025

Revised: 25 July 2025

Accepted: 31 July 2025

Published: 5 August 2025

Citation: Borzutzki, K.; Börner, M.; Fromm, O.; Rodehorst, U.; Winter, M. Process–Structure–Property

Correlations in Twin-Screw Extrusion of Graphitic Negative Electrode Pastes for Lithium Ion Batteries Focusing on Kneading Concentrations. *Batteries* **2025**, *11*, 299. <https://doi.org/10.3390/batteries11080299>

Copyright: © 2025 by the authors. Licensee MDPI, Basel, Switzerland. This article is an open access article distributed under the terms and conditions of the Creative Commons Attribution (CC BY) license (<https://creativecommons.org/licenses/by/4.0/>).

Keywords: lithium ion battery; electrode manufacturing; electrode paste processing; continuous mixing; extrusion

1. Introduction

To replace fossil fuels with natural fluctuating renewable energy sources, a reliable, cost-effective, and efficient technology for electric energy storage is inevitable. In this regard, batteries are applied in various stationary and particularly portable and (auto)mobile applications such as electric vehicles (EV) [1–5]. Presently, lithium ion batteries (LIBs) are dominating the market, where commercial state-of-the-art cell systems are comprised of a graphitic negative active material (Gr) and a positive active material (e.g., LiFePO₄ or Li(Ni_xMn_yCo_z)O₂, NMC, $x + y + z = 1$) [6,7]. Still, increasing consumer demands for high-performance and simultaneously low-cost batteries need to be fulfilled to assert these technologies on the market. Within the process of battery cell production, roughly 70% of

the overall costs can be related to material costs, while 30% are attributed to production costs [8,9].

In addition to the development of innovative material systems, reducing production costs through improved process efficiency and lowered consumption of materials and energy is a key priority for future large-scale battery manufacturing [10].

Among the various steps involved, the mixing process plays a crucial role, as its effectiveness significantly impacts the characteristics of the resulting electrode slurry. This, in turn, affects the subsequent process steps, particularly coating and drying, as well as the electrochemical performance of the final electrodes, including their cycle life and ability to support fast charging [8,11,12].

During mixing, active materials, binders, and conductive agents need to be thoroughly de-agglomerated, uniformly distributed, and dispersed without causing damage to the particles or leaving any agglomerates behind. Therefore, careful adjustment of process parameters, including an appropriate configuration of the mixing equipment, such as the extruder setup, is essential to achieve high-performance electrode paste and battery cells [13–15].

Currently, the industrial standard for producing electrode pastes is a batch process [15]. This method provides high flexibility that is beneficial, especially when working with limited quantities of novel materials or testing various formulations. However, in mass production environments, batch processing can be inefficient due to the time and material loss associated with cleaning and switching between different material systems [16,17]. In contrast, continuous mixing processes are considered an attractive alternative with respect to large-scale production in industry. Such technologies allow for the continuous production of electrode pastes with consistently high quality. By considering the processing of established materials, a substantial reduction in production times due to considerably lower residence times and correspondingly less energy consumption during the process as well as reduced scrap due to reduced necessity for cleaning compared to batch-based processing is achieved [8,9]. Particularly, twin-screw extruders have recently been introduced as an innovative mixing procedure for electrode fabrication.

For this particular application, significant economic and energetic benefits can be achieved using continuous processing compared to batch-type processing. According to data from a machine manufacturer, the energy consumption for producing one ton of electrode slurry can be reduced from approximately 224 kWh in conventional batch mixing to just 56 kWh with extrusion-based processing, amounting to energy savings of about 75% [18]. This highlights the relevance of extrusion technology not only for process efficiency but also for sustainable, large-scale battery production.

In twin-screw extruders, two corotating screws are responsible for processing the material along a process zone. It is a continuous process, as the initial materials are continuously dosed in this process zone, and the final product continuously flows out of the outlet at the end of the machine (as depicted in Figure 1) [19]. An important feature of the twin-screw extruder is the modular design of the screws. These consist of a core shaft and screw elements that can be arranged and coordinated variably. There are different elements for different purposes. On the one hand, there are conveyor elements that look like screws. These draw in a product and transport it in the process direction toward the extruder outlet. Kneading elements, made up of several kneading disks that are offset to each other, are used, among other things, to mix the product distributively (homogenizing the compounds) and dispersively (de-agglomerating the particles). Return elements are also helical in design, but in the opposite direction, so that the product is pushed back into the extruder against the process direction and accumulated. By configuring certain screw compositions and by flexibly placing the feed points for the addition of materials at

different positions along the extruder, different process zones can be installed. Materials can be added directly at the beginning of the process zone or at certain areas in the middle or at the end of the process zone, whereby their load can be adapted, and different process steps and zones can be created (see Figure 1) [19].

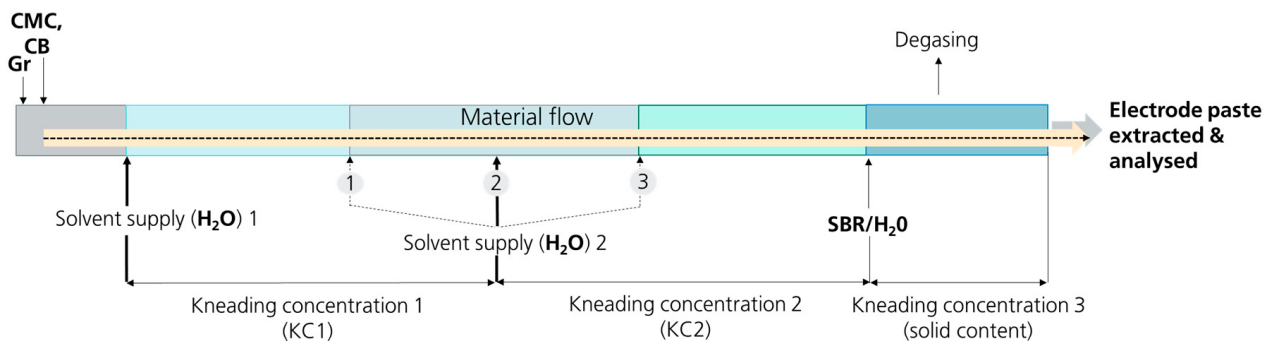


Figure 1. Setup of the extruder. The supply of the powders Gr, CMC, and CB takes place at the beginning of the process zone, followed by the first supply of the solvent. The second solvent supply can be varied along the process zone to shorten or elongate the kneading zone 1 (zone with kneading concentration 1). SBR is added at the end of the process zone prior to the degassing step via a vacuum pump and the outlet of the process zone, where the electrode paste is extracted.

Due to the high degree of process flexibility, it is possible to react flexibly to changes in the tasks, the process, or the desired product properties.

Nevertheless, while extruders are well established and deployed in food and polymer industries, experiences in the battery industry are rather limited [9,19]. However, since the process parameters from the established fields of application cannot be adapted to the requirements of the complex multi-component system of electrode pastes, a direct transfer to this new field is not trivial and requires comprehensive process studies.

In the field of extrusion-based processing of electrode pastes, only a few studies exist, which mainly focus on developing the process on small scales for positive electrode compositions (e.g., surface coated, high Ni materials, different binder (PVDF), and solvent (NMP) compared to negative electrodes) [8–10,15,20]. Beyond this, previous studies have mainly focused on variation in the solid content of the electrode paste [8,15], throughput [9], screw speed [9,10,20], and screw configuration [9,10], while the kneading concentration was neither discussed nor applied as a relevant parameter since only one solvent supply was used in the setup of the process. In a single study producing electrode flakes for quasi-solid production, the benefit of adding the solvent in a later state to the extruder was mentioned, but the criticality of this process parameter not investigated in detail [21]. Nevertheless, based on extensive studies on the batch-type mixing, stepwise addition of the solvent is considered beneficial with respect to optimal de-agglomeration of the carbon black and thus with respect to the final cell performance [22,23].

A deep understanding of the process and process-product correlations is essential to adapt the process efficiently to new materials or material compositions (e.g., Na-based, new binder materials, varying particle sizes, ...) and to predict scaling effects and, correspondingly, reduce ramp-up times for industrial plants. Thus, process know-how in the field of extrusion of electrode pastes still needs to be developed to widely establish continuous mixing processes in industrial large-scale fabrication lines.

Even though the modular design of extrusion lines (particularly the screw configuration) offers a large scope for parameter variation and allows us to specifically design and adapt the process to material and product characteristics, this variety also constitutes a major challenge in developing optimum process conditions. Thus, to gain a comprehensive understanding of the mixing process, intense studies applying different active materials

and electrode paste compositions, as well as variations in processing parameters, to decipher their influence on the electrode paste characteristics are inevitable. Therefore, in this study, an innovative continuous mixing process using a twin-screw extruder was used for parameter variations in the production of graphite-based aqueous negative electrode formulations for high-power applications of LIBs.

Within the frame of process optimization and development, a preliminary study was performed by the authors (not published and not part of this manuscript but summarized in a table in the Supplementary Materials, Table S1) to identify the criticality of the multiple process parameters. Various other process parameters were varied in specific ranges (screw speed from 800 to 1200 rpm, solid content from 40 to 65 wt%, throughputs from 30 to 150 kg/h, kneading concentration from its minimum (defined by the solid content of the paste) to its maximum (defined by process limitation), kneading zone length, and screw configuration). In this preliminary study, it was found that, within the range of throughputs and screw speeds, the characteristics of the electrode pastes are rather comparable. Although a significant increase or decrease in the screw speed will surely yield either insufficient dispersion/de-agglomeration or enhance the effects of material destruction due to in-/decreased residence times and/or lower/higher shear rates applied to the material, a wide range of processing parameters can be applied to achieve a stable process. Changing the solid content is a suitable method for adapting properties of the electrode paste, though it is not a process-related adaptation. Changing the screw configuration is a powerful but complex and time-intensive possibility for adaptation of the electrode paste characteristics. Variation in KC1 (local solid content in the process zone; see Section 2.2 Equation (1)), however, allows us to change the properties of the electrode paste systematically and allows for simple adaptation of the electrode paste properties. Based on these observations (presupposing that the other process conditions are in a suitable range), the first kneading concentration (KC1) is identified as one of the key parameters that allows for systematic and rather simple adaptation of relevant properties of the electrode paste. Thus, this study highlights the criticality of KC1 and presents its impact on the microscopic and macroscopic levels.

Varying KC1 systematically, a detailed analysis of the electrode pastes, the produced electrodes, and the associated electrochemical performance in LIB cells allows us to reveal the underlying effects on the material level and fundamental correlations. A process limit in terms of unintended material degradation is identified at elevated KC1, and it is revealed how different phenomena (material degradation and carbon black de-agglomeration) interact in this multi-compound system and how they impact the final electrochemical characteristics of a cell. Thus, optimal process parameters consist of identifying a sweet spot between the occurring phenomena. Finally, process–property relations for the extrusion process are identified. In particular, it is demonstrated how the machine parameter of engine power that is tracked during the process correlates with the characteristics and quality of the electrode paste analyzed by offline measurements. Thus, monitoring these process parameters allows for indirect control of the quality of the electrode paste.

2. Materials and Methods

2.1. Materials

For production of the electrode pastes by extrusion-based processing, two types of synthetic graphite active materials (particle size distributions shown in Figure S1, Hitachi Chemicals, Tokyo, Japan, Gr1: $D_{mean1} = 10.5 \mu\text{m}$, BET surface: $1.7 \text{ m}^2/\text{g}$, Gr2: $D_{mean2} = 9 \mu\text{m}$, SBET surface: $3.9 \text{ m}^2/\text{g}$) were used as active material, with carboxymethyl-cellulose (CMC, 30k (molecular weight: 30.000 g/mol), Dupont DP Specialty Products, Germany, GmbH & Co. KG, Neu-Isenburg, Germany) and styrene–butadiene rubber (SBR,

BM–451B, Zeon Europe GmbH, Düsseldorf, Germany, 40 wt% SBR in H₂O, particle size average = 145 nm) as polymeric binder materials and carbon black (CB, Super C45, Imerys Graphite & Carbon Belgium SA, Willebroek, Belgium, BET surface area = 46.9 m²/g) as conductive additive. Copper (Cu) foil of 10 µm thickness (Circuit Foil Luxembourg, Luxembourg) was used as a current collector. All compounds were used as received without further purification.

2.2. Extrusion-Based Fabrication of Electrode Pastes

Electrode pastes were fabricated by a twin-screw extrusion line (BCTM30, Bühler Group, Uzwil, Switzerland). The negative electrodes consisted of 95 wt% graphite, 2 wt% SBR, 2 wt% CMC, and 1 wt% carbon black. Two different types of electrode paste with equal composition but different synthetic graphite materials were produced. The solvent was deionized water. The setup of the extruder is schematically presented in Figure 1. Initially, the powder compounds are inserted into the process zone, followed by the first supply of the solvent (deionized water). The second water supply can be varied along the process zone to change the length of the first kneading zone (zone between the first and second water supply). Within this zone, the so-called kneading concentration 1 (KC1), defined as the local solid content, is adjusted based on the amount of water inserted into the extruder at the first solvent supply. The kneading concentration 1 can be calculated as follows:

$$KC1 = \frac{w_{\text{solid}}}{w_{\text{solid}} + w_{H_2O@\text{solvent supply}1}} \quad (1)$$

with w_{solid} being the amount of all solids/powders (Gr, CMC, and CB) in wt%, and $w_{H_2O@\text{solvent supply}1}$ being the amount of solvent (H₂O) that is added at solvent supply 1 (see Figure 1) in wt%. Note that the overall solid content of all electrode pastes extracted from the experiments was set to 50%. In addition, the amounts of Gr, CMC, CB, and SBR are kept constant for all experiments within this study. Therefore, to adjust KC1, the ratio of solvent, which is inserted at positions 1 and 2, is varied in order to vary the kneading concentration (e.g., for KC1 = 55%, the local solid content within the first process zone prior to solvent supply 2 is 55%, which can be realized by adding most of the amount of solvent at solvent supply 1, while only a little amount of solvent is added to solvent supply 2 to reach a final solid content of 50%). For higher KC (KC > 55%), the amount of solvent added at solvent supply 1 is decreased, thereby increasing the local solid content in the first process zone, while the amount of solvent added to solvent supply 2 is increased.

In this work, the second solvent supply and, thus, the end of kneading zone 1 is located at position 1, 2, or 3. Due to the comparably low mechanical stability of SBR, the SBR binder suspension (40 wt% in water) is added at the end of the process zone. Finally, a degassing step via vacuum pumps is performed just before the outlet of the electrode paste. All experiments were conducted at 20 °C, which was monitored and controlled by a cooling system along the process zone. The screw configuration was kept constant within this study to allow systematic analysis of the impact of a variation in process parameters on the characteristics of the electrode pastes and corresponding electrodes. Generally, the screw configuration for electrode pastes is composed such that the different process zones are represented, allowing for dispersive mixing at the beginning of the process zone and distributive mixing close to the extruder outlet. Thus, the first process zone (KC1) contains an intensive kneading zone, including kneading and backwinding elements, while the second process zone (KC2) contains less intensive kneading elements, and KC3 is composed mainly of forwarding elements for low energy input homogenization of the final electrode paste. Process capability and reproducibility of the extrusion process have been validated by fabricating equal electrode pastes (identical solid content, machine parameters, and

recipe) multiple times (within the time frame of several months) with equal results of the shear rate-dependent viscosity, as demonstrated in Figure S2.

2.3. Fabrication of Electrodes

The electrode slurries were cast onto a Cu current collector foil using a doctor blade technique. A gap width of 80 μm to 200 μm was used to achieve a mass loading of 7 mg cm^{-2} , corresponding to an areal capacity of 2.35 mAh cm^{-2} at a determined practical capacity of 355 mAh g^{-1} for the used graphite materials. The obtained electrodes were dried at 60 $^{\circ}\text{C}$ overnight, followed by further drying at 80 $^{\circ}\text{C}$ under reduced pressure (10^{-3} mbar) vacuum.

2.4. Characterization

2.4.1. Rheology

The viscosity of the electrode pastes produced was recorded at 20 $^{\circ}\text{C}$ using a rheometer (RheoCompass, Anton Paar) at shear rates between 10^{-2} and 10^4 s^{-1} with four measurement points per decade without pre-shear.

2.4.2. Particle Size Analysis (PSA)

To obtain a quantitative result of the particle size distribution, a laser-based scattering analysis was performed using a Particle Size Analyzer from Anton Paar. For this purpose, a spatula tip of the electrode paste was placed into the sample container (yielding a transmission of 30% of the laser beam) with a small amount of surfactant. The particle size distribution was determined in the range of 10 $^{-2}$ μm to 500 μm .

2.4.3. Scanning Electron Microscopy (SEM)

Scanning electron microscopy was performed with a Zeiss Auriga cross-beam workstation (Carl Zeiss Microscopy GmbH). For surface analysis, an accelerating voltage of 3 kV was applied.

2.4.4. Electrochemical Investigations

For electrochemical investigations, two electrode coin cells were assembled in a dry room ($\text{H}_2\text{O} < 20 \text{ ppm}$, dew point below $-60 \text{ }^{\circ}\text{C}$). For analysis of Gr II Li cells, metallic lithium (GELON LIB Group) and graphite-based electrodes were punched to $\Phi 12\text{mm}$ and assembled in 3-electrode Swagelok cell setups. To avoid dendrite penetration, six layers of polyolefin, non-woven (Freudenberg 2190), were used as a separator stack, and 1M LiPF₆ in ethylene carbonate (EC) and ethyl methyl carbonate (EMC; EC:EMC = 3:7 wt.) with 2 wt% vinylene carbonate (VC) (E-Lyte) were used as electrolytes. In the case of NMC622 II Gr cells, NMC622-based positive electrodes were punched to $\Phi 14\text{mm}$, while the negative electrode disk was $\Phi 15 \text{ mm}$. The positive electrodes were produced at the MEET Battery Research Center, Münster, Germany, battery line with 93 wt% LiNi_{0.6}Mn_{0.2}Co_{0.2}O₂ (NMC622, BASF), 3 wt% PVDF (Solef, Solvay, Brussels, Belgium) as binder, and 2 wt% CB (SuperC65, Imerys Graphite & Carbon), as well as 2 wt% conductive graphite (KS6L, Imerys Graphite & Carbon). The total mass loading was set to 12.5 mg cm^{-2} , corresponding to an areal capacity of 2.1 mAh cm^{-2} at a practical capacity of 180 mAh g^{-1} for NMC622 (N:P ratio of the cells was 1.15:1). A polypropylene monolayer (Celgard 2500) was used as separator and 1M LiPF₆ in EC:EMC (3:7 wt.), and 2 wt% VC was used as electrolyte.

Cycling investigations were performed using a Maccor (Tulsa, OK, USA) 4000 battery analysis system at 20 $^{\circ}\text{C}$. For analysis of Li || Gr cells, an asymmetric procedure utilizing a 0.05C discharge (corresponding to lithiation of the Gr layers) and 0.5C charge rate (delithiation of Gr) within a voltage range of 0.02 V to 1.5 V was applied. In the case of the analysis of the long-term charge/discharge cycling stability and rate capability, NMC622 || Gr cells

were cycled in the voltage range of 3.0 V to 4.3 V (constant current, CC), and a symmetric procedure was applied. In the case of long-term cycling investigations, 3 initial cycles were performed at C/10, while 1C was used for all subsequent cycles. The procedure for analysis of the C-rate performance was set up using 3 cycles each at C/10, C/5, C/2, 1C, 2C, and 3C. For all samples, 3 cells were built, and mean values and standard deviations are presented in the graphs.

2.4.5. X-Ray Diffraction (XRD)

Samples for X-ray diffraction (XRD) measurements were prepared by scraping the electrodes off the copper current collectors or using the pristine Gr powder material. The obtained powders were sealed in 0.5 mm diameter glass capillaries for X-ray diffraction measurements. These were spinning during the measurements in the transmission/Debye Scherrer geometry in order to reduce the effects of preferred orientation. Data collection was carried out at room temperature on a STOE STADI P, Darmstadt, Germany, diffractometer [Mo K α_1 radiation; $\lambda = 0.7093 \text{ \AA}$; a curved Ge(111) monochromator; two Mythen 2K detectors]. Data were collected in 0.015° steps in 2θ . Similarly, LaB₆ 660c NIST® was measured and used as a standard for reflection line shape in Rietveld analyses with Topas® 7 (Bruker AXS, Karlsruhe, Germany) to model the instrumental line broadening.

3. Results and Discussion

3.1. Impact of the Kneading Concentration on Critical Parameters of the Electrode Pastes

The kneading concentration is one of the most important parameters that can be varied to modify the characteristics of an electrode paste. Particularly, the viscosity of the final electrode paste needs to be adapted to the subsequent coating process (different techniques like doctor blade, comma bar, and slot die) as well as to the corresponding process parameters (e.g., coating speed, coating thickness, etc.). Thus, KC1 is a powerful parameter to optimize the extrusion process toward high-quality electrode pastes tailored for further processing. In the following discussion, the focus lies on the results obtained for variations in KC1 at constant kneading length (second water supply being fixed at position 2, as indicated in Figure 1), while the impact of varying KC1 toward longer and shorter kneading zones (solvent supply 2 at position 1 or 3) is discussed shortly, and the corresponding results are presented in the SI. KC1 varies in a range from 55% to 85% for two different graphite materials, Gr1 and Gr2, which differ in their particle size distribution, as demonstrated in Figure S1. As one of the most important characteristics of electrode pastes, their rheological behavior was analyzed. Figure 2a,b present the shear rate-dependent viscosities of the final electrode pastes extracted at the extruder outlet for both materials and different KC1s.

All curves display a typical behavior for electrode pastes, including a “transient viscosity hill” for low shear rates [24,25] (roughly $< 10^{-1} \text{ s}^{-1}$), followed by a shear thinning behavior for shear rates $> 10^{-1} \text{ s}^{-1}$. Since shear rates between 10^{-1} and 1000 s^{-1} are applied to the pastes during coating (depending on the coating technique and specific coating parameters), lower viscosity values at higher shear rates allow for sufficient processability. In addition, comparably high viscosities at low (or zero) shear rates facilitate stagnation of the paste’s flow after application on the current collector foil. With respect to the produced electrode pastes using Gr1 and Gr2, all samples yield sufficient quality for further processing within the range of applied KC1. Furthermore, for both materials, the viscosity curves initially decrease with increasing KC1, which can be explained by an increasing dispersion efficiency due to an increase in energy input. This decrease occurs up to a certain reversal point, marking the processing limit at 82.5% KC1 in the case of Gr 1 and 80% KC1 in the case of Gr 2. Beyond this limit, a further increase in KC1 results in an increase in

viscosity, indicating a change in rheology that might be associated with detrimental effects with regard to the interactions (e.g., particle–particle, particle–binder, and particle–solvent) of the components of the electrode paste. Additionally, analysis of the machine parameters reveals that the observed trend in viscosity inversely correlates with the engine power of the extruder (reaching its maximum at KC1 = 82.5% for Gr1 and KC1 = 80% for Gr2), as demonstrated in Figure 2c,d by plotting the inverse viscosity at a shear rate of 1 s^{-1} and the engine power as a function of the KC1. The engine power corresponds to the power consumed by the extruder to reach the rotation speed of the screws set by the user while material is processed. This energy is then normalized to the throughput (Wh/kg) in order to compare the energy efficiency of different processing parameters (e.g., optimizing a process with respect to energy consumption) or to compare the extrusion process to other mixing technologies, e.g., batch-type mixing.

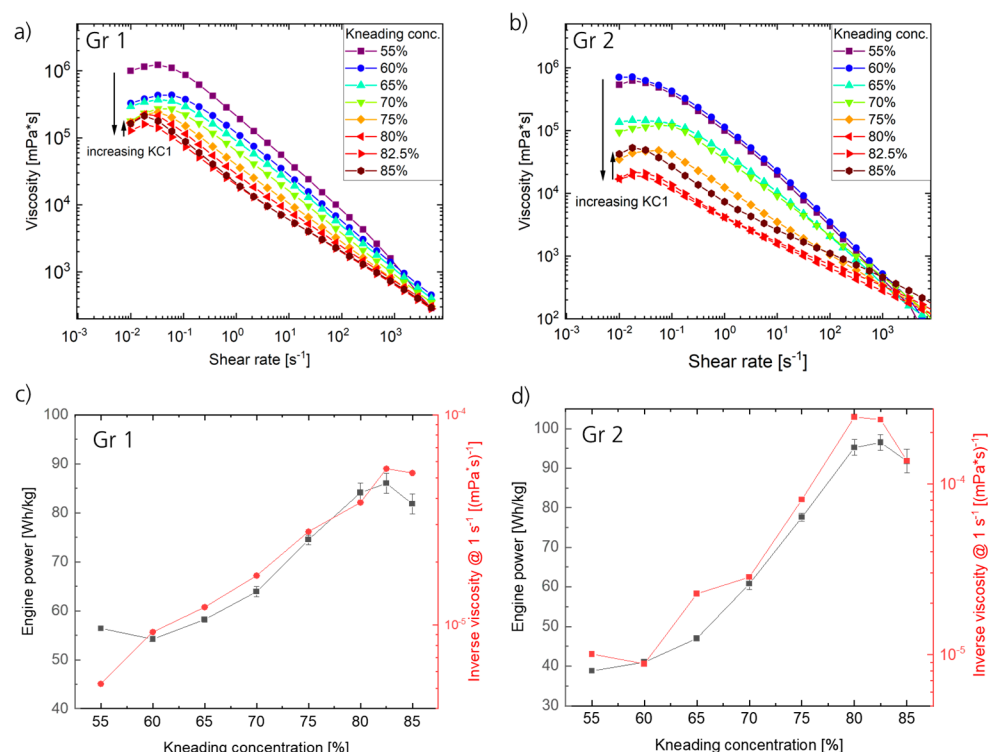


Figure 2. (a,b) Viscosity curves for negative electrode suspensions (final outlet of the extruder) with (a) Gr1 and (b) Gr2 as active materials and different kneading concentrations in the first kneading zone. (c,d) Engine power and inverse viscosity @ 1 s^{-1} depending on the kneading concentration.

Note that the progression of the inverse viscosity over KC1 is independent of the chosen shear rate, as the observed correlations are equal for viscosities at different shear rates (shown in Figure S3). For both materials, an increase in engine power was identified with increasing KC1 and decreasing viscosity. This correlation was expected since increasing the energy input to the process zone results in a more effective mixing, associated with a lower viscosity of the electrode paste.

Both the behavior of the viscosity curves within the applied range of KC1 as well as the correlation of inverse viscosity and engine power were similarly obtained in the case of varying the kneading zone length (solvent supply 2 at positions 1 and 3, respectively; see Figures 1 and S4). However, it occurs that the observed behavior becomes more pronounced with the increasing length of the kneading zone, which is plausible since the material is processed for a longer duration at high solid contents. Thus, the overall stress applied to the particles is enhanced compared to the shorter kneading zone length due to strong material–screw interaction, yielding a strong mixing (or grinding) efficiency.

Consequently, monitoring the machine parameters within initial process optimization at varying KC1 and zone lengths is crucial and allows the prediction of changes in the electrode paste characteristics indirectly. In this way, relevant mechanisms that occur beyond certain processing limits can be detected in line, even without direct determination of the properties of the electrode paste.

In addition to the occurrence of a reversal point/processing limit, a variation in the shape of the shear rate-dependent viscosity curves occurs. For all curves ranging from a KC1 of 55% to 70%, an almost linear behavior of the viscosity (in a double logarithmic plot) is observed within the range of 0.1 s^{-1} to 1000 s^{-1} . At $\text{KC1} > 80\%$ for Gr1 and $\text{KC1} > 75\%$ for Gr2, however, the rheological behavior in this range changes toward a downward bend curve. Generally, the progression of shear rate-dependent viscosity curves represents the interaction of solid compounds within the processing solvents of the electrode paste and might be related to the polymer–particle network, particle bridging, etc. [26]. Previous studies have demonstrated the influence of material properties such as molecular weight or concentration of polymeric binders (e.g., CMC) [27–29] and of the size and shape of graphite particles [30] on the rheological characteristics of the electrode pastes. With regard to the observed progression and changes in dependence of the process parameters (KC1) of an electrode paste composed of multiple components, various reasons might cause the observed deviation of the linear shear thinning behavior. The change in the shape of the curves (at KC1 of 75–80%) arises prior to the occurrence of the reversal point at 80% to 82.5%. Therefore, it can be assumed that there are two phenomena present during the extrusion process that influence the rheological behavior independently.

For further investigation, particle size distributions of the electrode pastes, which allow us to identify phenomena such as (de-)agglomeration and potential particle degradation occurring during the mixing process, were performed. Figure 3a,b display the particle size distributions of the two graphite-based compositions for different KC1.

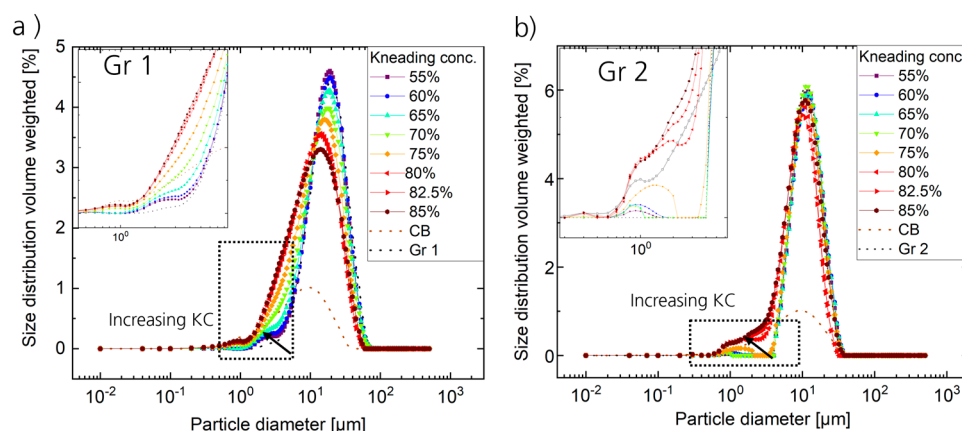


Figure 3. Particle size distributions of different negative electrode suspensions utilizing (a) Gr 1 and (b) Gr2 and different kneading concentrations in the first kneading zone.

For both materials, a shift in the distribution toward lower particle sizes can be observed with increasing KC1 (the maximum of the mode for Gr1 occurs at $18.9\text{ }\mu\text{m}$ for $\text{KC1} = 60\%$, $16.5\text{ }\mu\text{m}$ for $\text{KC1} = 70\%$, and $14.6\text{ }\mu\text{m}$ for $\text{KC1} = 85\%$ and for Gr 2 at $11.90\text{ }\mu\text{m}$ for $\text{KC1} = 60\%$, $11.46\text{ }\mu\text{m}$ for $\text{KC1} = 70\%$, and $11.06\text{ }\mu\text{m}$ for $\text{KC1} = 85\%$). Particularly, in the case of higher KC1 starting from $\text{KC1} = 70\%$, in the case of Gr 1 and $\text{KC1} \geq 75\%$, and in the case of Gr 2, a noteworthy shift in the left shoulder of the distribution within the particle size distribution to lower values in the range of $1\text{--}10\text{ }\mu\text{m}$ and an increasing fraction of particles with a diameter of slightly below $1\text{ }\mu\text{m}$ is observed. Probably, the growth of the small mode can be correlated to an extended de-agglomeration of carbon black (see

Figure S1) since the distribution of the raw CB material shows a bimodal distribution at around 10 μm and near 1 μm due to different sizes of CB agglomerates, while the raw materials Gr 1 and Gr 2 do not contain particles lower than 4–5 μm . In addition, the overall shift in the distributions toward smaller particle diameters points toward particle grinding of the Gr materials at high KC1 of $\geq 75\%$ in the case of Gr1 and $\geq 80\%$ for Gr2. This effect is more pronounced in the case of Gr 1, which can be explained by the overall smaller particle sizes of Gr2 compared to Gr1 (Gr1: $D_{90} = 35.4 \mu\text{m}$, $D_{50} = 17.4 \mu\text{m}$ and Gr2: $D_{90} = 20.0 \mu\text{m}$, $D_{50} = 11.1 \mu\text{m}$; see Figure S1). Due to the fixed shear gap (gap between the screws) as well as the gap size between screws and machine housing, larger particles will be ground prior to smaller particles.

Based on these results, probably with increasing KC1, progressing de-agglomeration and slight grinding of the active material take place. The mixing efficiency increases up to the process limit at KC1 = 70%. At this point, ideal mixing is achieved with only marginal grinding and sufficient CB de-agglomeration. Increasing KC1 further promotes particle grinding and CB de-agglomeration such that ideal mixing is surpassed, yielding a change in the shape of the viscosity curves and finally even a rise in the viscosity values, probably when grinding predominates mixing within the process.

Nonetheless, while analysis of the electrode paste gives important information and hints on fundamental phenomena on the microscopic level, they are insufficient to gain a comprehensive understanding and evaluate the impact of the observed phenomena. It is noticeable that the observed trends (e.g., change in the shape of the shear rate-dependent viscosity as well as the occurrence of the reversal point/processing limit, the correlation of viscosity, engine power, shifts in PSA curves, and the growing mode at small particle sizes) generally occur reproducibly for different graphite particle morphologies irrespective of the particle size distribution of the initial material. Therefore, for further analysis of the process–product correlations, electrode fabrication and comprehensive studies are presented for electrodes prepared from electrode pastes using Gr1 (as a representative material).

3.2. Impact of the Kneading Concentration on Electrode Characteristics

KC1 not only affects the rheology and particle size distribution of the electrode paste. It also has a decisive influence on the resulting electrode characteristics and their electrochemical performance. Thus, electrode pastes processed with KC1s of 60%, 70%, and 85% were coated and analyzed in detail. Figure 4 shows the surface morphology of the coated (non-calendered) electrodes based on Gr1 and fabricated at different kneading concentrations (60%, 70%, and 85%). In addition, the porosity \mathcal{E} of the non-calendered electrodes was calculated based on

$$\mathcal{E} = 1 - \frac{m_{area}}{L} \left(\frac{w_{AM}}{\rho_{AM}} + \frac{w_{B1}}{\rho_{B1}} + \frac{w_{B2}}{\rho_{B2}} + \frac{w_{CB}}{\rho_{CB}} \right) \quad (2)$$

where m_{area} is the total mass loading of the electrodes, L is the thickness of the electrodes, w is the amount in weight percent of active material (AM), binder ($B1 = \text{CMC}$ and $B2 = \text{SBR}$), and carbon black (CB), and ρ is the density of the corresponding compounds ($\rho_{AM} = 2.24 \frac{\text{g}}{\text{cm}^3}$, $\rho_{CB} = 1.60 \frac{\text{g}}{\text{cm}^3}$, $\rho_{CMC} = 1.59 \frac{\text{g}}{\text{cm}^3}$, $\rho_{SBR/H2O} = 1.00 \frac{\text{g}}{\text{cm}^3}$) of the electrode paste.

In Figure 4, it can be observed that, with increasing KC1, Gr particles appear smaller and more densely packed on the electrode surface, as indicated by the decrease in porosity of as-prepared electrodes with increasing KC1, while CB chains or agglomerates appear smaller. In addition, the shape of the graphite particles tends to change from a rather round “potato”-like to a more edged and “flake”-like shape.

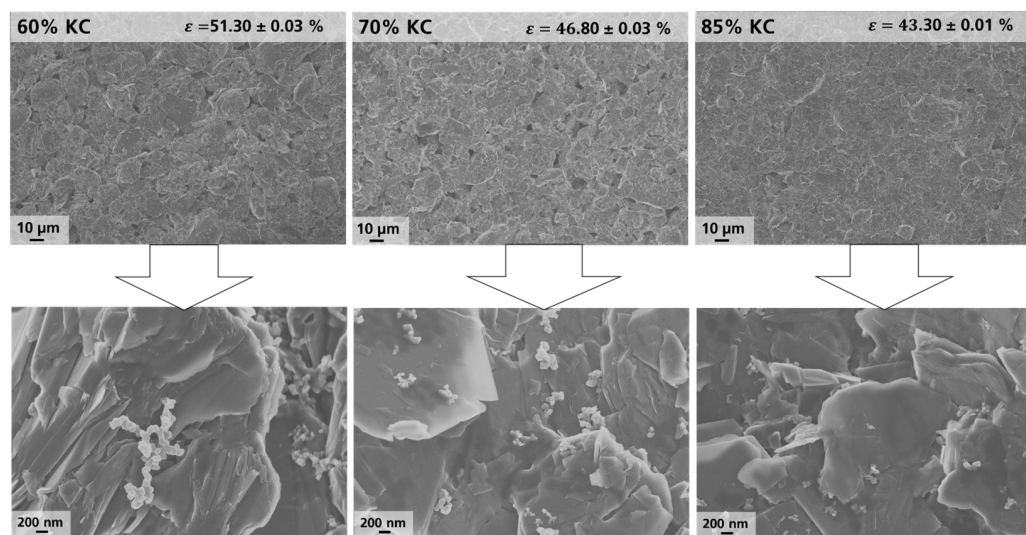


Figure 4. Scanning electron microscopy (SEM) images and calculated porosities of electrode surfaces coated with graphitic electrode pastes produced by extrusion with KC1s of 60%, 70%, and 85%.

These observations were confirmed by analysis of multiple spots on the electrode surface (see also Figures S5 and S6). These observations correlate well with the shift in the main mode of the particle size distribution (Figure 3a) toward lower values (as pointed out for the variation in the maxima of the modes in Section 3.1) accompanied with a broadening of the distribution, in addition to an increase in the intensity of the mode at $\sim 1 \mu\text{m}$, attributed to CB de-agglomeration (inlet in Figure 3a). Thus, based on combined PSA and SEM analysis, it can be concluded that active Gr particles are ground, and CB becomes notably more de-agglomerated at higher KC1 due to an enhanced energy input. These observations are in good agreement with recent studies, where a similar behavior in the case of variation in the kneading concentration for batch-type mixing was identified [24,31]. It was presented that enhanced KC1 yields a broadening of the particle size distribution associated with abrasion of graphite particles and breakage of CB agglomerates, which results in a higher packaging density on the electrode level, which was demonstrated by a reduced porosity and an increase in tortuosity of non-calendered electrodes. Thus, the results obtained in this study indicate a direct transferability of phenomena in both batch-type and continuous mixing, even though both processes and corresponding process parameters differ in several aspects.

Correlating these observations to the rheological behavior discussed in the previous Section 3.1 (Figure 2), it can be deduced that both the grinding of the graphite particles and the change in the CB chain/agglomerate size cause a change in rheological properties and particle size distribution. It is likely that the particle shape influences the flow behavior of the electrode pastes for varying shear rates. Flake-like particles may align in preferential matters [24] (e.g., horizontally), which is likely to occur under application of certain shear rates (in this case between 10^{-1} s^{-1} and 10^2 s^{-1} ; see Figure 2), causing a decrease in the viscosity in this region. Probably, a jump of the whole curve (after having reached the reversal point, e.g., a processing limit at a certain KC1) may occur when excessive grinding yields a critical amount of small particles associated with a considerably larger surface area (accompanied by strong CB de-agglomeration, probably surpassing the optimum degree).

However, the characterization via SEM and PSA only allows us to analyze the particles within the electrode paste, while phenomena that might occur due to changes in the CMC polymer chains, such as chain length or entanglement, cannot be revealed. Note that SBR dosing and process parameters after solvent supply 2 (Figure 1) are identical in all experiments; hence, changes in the SBR polymer chains are excluded.

In order to exclude the effect of specific electrode paste compounds, further experiments with varying compositions and elimination of 1) CMC and 2) CB are conducted. It is expected that the phenomena (curvature of the shear rate-dependent viscosity at high KC1) would not occur in one of these modified pastes if they were related to either of the materials (CMC binder or CB). Rheological analysis of the electrode paste containing 4 wt% of CMC (instead of 2 wt%) produced with a high KC1 of 85% (see Figure S7b) reveals that the curvature of the shear rate-dependent viscosity is downward bent, similarly to the standard paste (Figure 2). Thus, a modification of CMC chains due to the enhanced shear rates at an enhanced KC1 can be excluded as a cause for the change in the curve's curvature (from linear to downward bent). Additionally, a paste without the addition of CB (0 wt% CB, see Figure S7a) was produced at KC1 = 70% and 85%. Also, in these cases, both of the viscosity curves display identical behavior compared to the standard paste (1 wt% of CB). Therefore, the observed change in the shape of the viscosity curve (Figure 2) can be related to the change in shape and size of the graphite material.

To further analyze the impact of different KC1s and of particle degradation on the crystal structure of the Gr materials, XRD measurements of the pristine Gr powder and the three different electrodes (KC1 = 60%, 70%, and 85%) were conducted. The XRD patterns are presented in Figure 5a. With processing and with increasing KC1s, several reflections at 19.6, 22.6°, 32.3°, 37.95°, 39.4°, and 39.7° increase in intensity, implying that a partial structural change in the Gr particles is initiated with increasing mechanical stress applied on the electrode paste. Rietveld refinement (specific data are presented in Table S2) was used to attribute the observed structural changes in the Gr particles. This analysis reveals that the observed changes can indeed be correlated to the graphitic structure since the observed reflections can be attributed to hexagonal and rhombohedral (less graphitic) [32] crystal structures, which are the two phases that are found in different ratios in all samples. As presented in Figure 5b, the initial Gr material majorly constitutes a hexagonal phase (97.8%), whereas only 2.2% represents a rhombohedral phase. As mechanical stress is applied to the material (during extrusion and increasing KC1), the content of the rhombohedral phase within the samples increases. The increase is rather slight (roughly by a factor of 2 to 4.1%) when processing the samples at KC1 of 60% as well as from 60% to 70% KC1 (again an increase by a factor of 2 to 8.2%), whereas for the sample prepared at 85% KC1, a relatively large fraction of 31.6% (a factor of 4 compared to KC1 = 70%) changes from a hexagonal structure toward a rhombohedral structure. Note that the obtained results predominantly represent changes in the Gr particle surface/edges due to the grinding of the Gr particles rather than the complete particle volume.

Consequently, in the case of a rhombohedral structure, the interlayer distance of the graphene layers is reduced to 0.208 nm compared to the initial hexagonal structure with 0.335 nm [33,34]. Based on previous studies, such a change in the crystal structure may be initiated by either the application of high temperatures, pressure [32,35,36], or mechanical forces [37]. In particular, it was stated that rhombohedral graphite can be obtained from initially hexagonal graphite by the application of unidirectional pressure associated with shear [38], which correlates well with the applied process conditions during the extrusion-based mixing. These previous studies were not conducted in the context of battery materials, and correlations of these structural changes with the electrochemical behavior were not investigated.

Although the presence of carbon black may influence the overall XRD signal, its low content (1 wt%) and the consistent trends observed in comparison to the pristine graphite suggest that the structural changes identified can be primarily attributed to the graphite component.

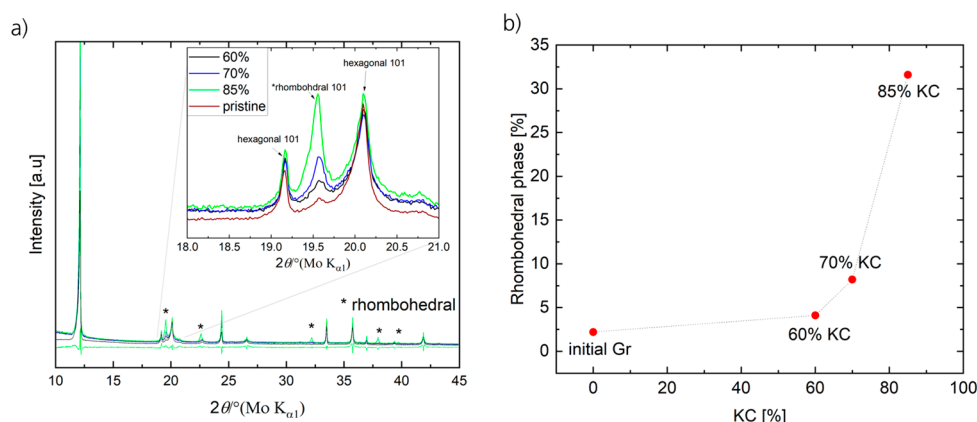


Figure 5. (a) XRD pattern of the initial Gr material and electrodes coated with electrode pastes produced by extrusion with different KC1s of 60%, 70%, and 85%. (b) Amount of rhombohedral phase (based on Rietveld refinement of the XRD measurements) for differently processed samples (pure Gr powder and different KC during extrusion).

3.3. Impact of the Kneading Concentration on the Electrochemical Cell Performance

In the previous section, the process–structure relations of KC1 and corresponding critical characteristics of the sub-product electrode paste and electrode were discussed. To fully determine the process–structure–property relations and to evaluate the specific influence of KC1, the electrochemical performance of the graphite-based electrodes was further investigated by the application of different cycling procedures in Gr II Li cells (for a detailed de-/intercalation study and the determination of specific capacities) and Gr II NMC622 cell setups for analysis of long-term cycling stability and rate capability.

Initially, the produced Gr electrodes were cycled against Li metal by applying a low lithiation rate of 0.05C for five cycles (delithiation at 0.5C) to identify the prominent stages of the intercalation process of graphite as present during charging of LIBs. Figure 6 displays the voltage profiles (a) and de-/lithiation capacity and Coulombic efficiencies (b) for electrodes containing electrode paste produced at 60% and 85% KC1.

Comparing the voltage profiles (Figure 6a) of samples processed at 60% and 85% KC1, the well-known staging mechanism of Gr is present in both cases and similarly pronounced in all cycles carried out, irrespective of the applied KC1. Corresponding dQ/dV plots confirming the presence of the staging mechanisms are presented in the Supplementary Materials in Figure S8.

In addition, similar specific discharge capacities (e.g., 337 mAh g^{-1} in the case of KC1 = 60% and 335 mAh g^{-1} in the case of KC1 = 85% in the first cycle) are obtained, indicating that the intercalation mechanism is maintained despite the formation of a rhombohedral graphitic structure on the particle surfaces and grinding effects, which do not influence the fundamental charging/discharging processes at low C-rates. However, the reduced interlayer distance at enhanced KC1 probably impacts the Li-ion mobility and thus the cell performance after multiple cycles, which will be further analyzed in the course of this paragraph.

With regard to the initial Coulombic efficiency (CE of first cycle, Figure 6b), the electrodes processed at 85% KC1 delivered a lower CE of 87.3%, compared to the 60% KC1 equivalent (CE of 94.4%). This difference was associated with the grinding effects (reduction in particle size compared to initial material and Gr particles processed at 60% KC1), resulting in an increased surface area and, correspondingly, a higher degree of electrolyte decomposition during SEI formation in the initial charge/discharge cycles. This interpretation is further supported by the dQ/dV analysis (Figure S8), which shows a more pronounced irreversible capacity in the 0.5–1.1 V region (where electrolyte decomposition

occurs) for the 85% KC1 sample during the first cycle. Within the subsequent cycles, the CE of both samples is similar (e.g., second cycle 98.5% for 60% KC1 and 98.7% for 85% KC1), indicating comparable amounts of electrolyte decomposition and effectiveness of the SEI, which, in turn, reflects that the structural changes at the surface have no visible influence on SEI formation. In the case of KC1 = 85%, a CE > 100% occurs at cycle 5. Probably, in the case of these samples (containing a denser morphology compared to the KC = 60% samples), at the initial cycles, in addition to SEI formation, lithium plating also occurs to a certain extent. Presumably, since Li plating is not a completely irreversible process, it can lead to a CE greater than 100 in the fifth cycle by reactivating the plated lithium.

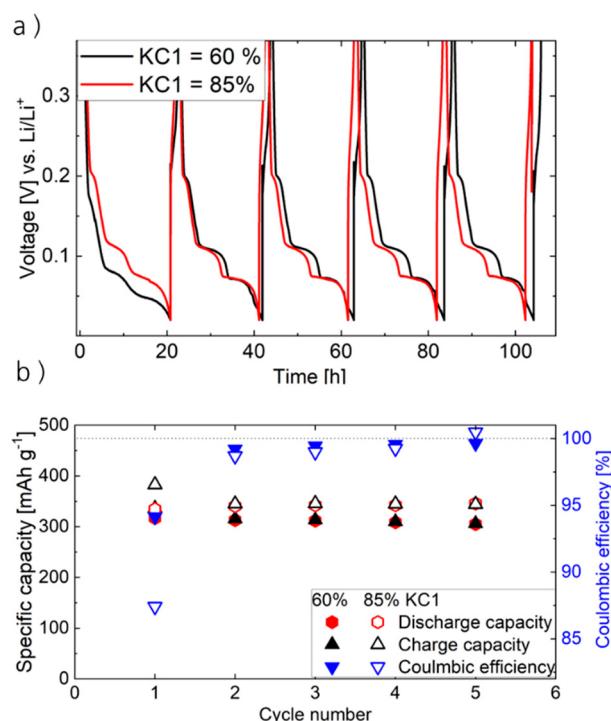


Figure 6. Electrochemical characterization of Gr II Li cells utilizing Gr-based electrodes produced from electrode pastes with 60% and 85% KC1. (a) Voltage profiles and (b) charge/discharge capacities and Coulombic efficiency for a representative cell cycled for 5 cycles at 0.05 C discharge and 0.5 C charge.

Figure 7 displays the long-term charge/discharge cycling stability and rate capability of the graphitic negative electrodes produced at 60%, 70%, and 85% KC1 in NMC622 ll Gr cells. Similar to Gr II Li setups, comparable initial specific discharge capacities were obtained at 0.1C for negative electrodes produced at different KC1. However, for subsequent charge/discharge cycles at constant or varying C-rates, the samples display distinct differences. Specifically, the capacity retention (Figure 7a) is reduced as KC1 increases. Particularly, within 100 cycles, in the case of KC1 = 60%, the capacity decays from $140.1 \pm 2.9 \text{ mAh g}^{-1}$ (cycle 4) to $121.5 \pm 10.1 \text{ mAh g}^{-1}$ @ cycle 104 (86.7%), while the capacity retention amounts to 83.6% in the case of KC1 = 70% (from $137.8 \pm 3.2 \text{ mAh g}^{-1}$ (cycle 4) to $115.3 \pm 10.1 \text{ mAh g}^{-1}$ @ cycle 104) and 74.0% in the case of KC1 = 85% (from $139.3 \pm 1.0 \text{ mAh g}^{-1}$ (cycle 4) to $103.1 \pm 13.2 \text{ mAh g}^{-1}$ @ cycle 104). This trend (similar to the CE in the case of Gr II Li cells) can be assigned to particle grinding at elevated KC1s and corresponding structural changes as well as an increase in surface area and subsequently enhanced electrolyte decomposition. Regarding the C-rate performance (Figure 7b), for higher rates of 2C and 3C, the poorest specific discharge capacities are obtained for KC1 = 60%, indicating insufficient de-agglomeration of CB (in agreement with the particle size distribution; Figure 3) and thus reduced electronic conductivity. In addition,

these samples display the highest deviations at high charge/discharge rates, which might be related to an insufficient mixing and homogenization of the compounds. However, to identify the limiting factor(s) within the electrode is not trivial since the electrode is a complex multi-compound system with various intercorrelating phenomena. Overall, an optimal network/distribution and sufficient contact areas between these compounds (also reflected by the porosity and tortuosity) will finally result in an optimal rate performance.

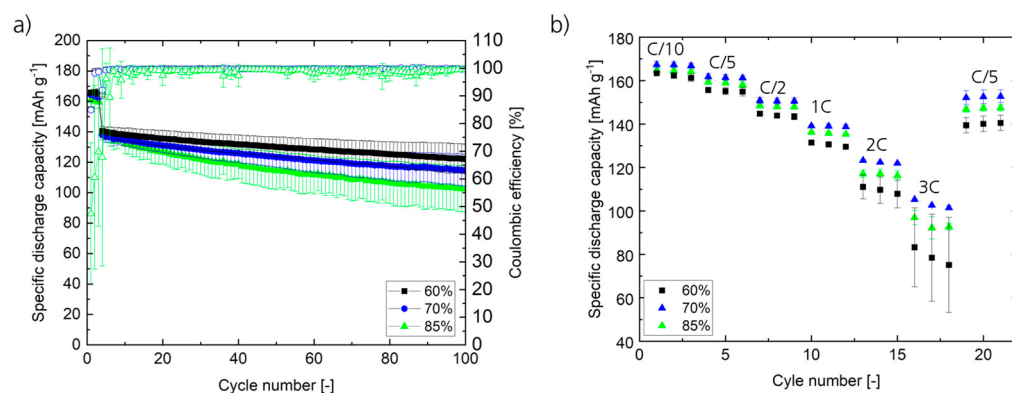


Figure 7. Electrochemical characterization of NMC622 ll Gr coin cells (constant current cycling) using the Gr-based electrodes coated with electrode pastes produced by extrusion with KC1s of 60%, 70%, and 85%. (a) Long-term cycling investigations. Initial 3 cycles were performed at 0.1 C and all subsequent cycles at 1C. (b) C-rate performance using a symmetric procedure and different rates as indicated in the graph.

Contrarily, the samples with the high KC1 of 85% show reduced rate capability compared to the medium KC1 of 70%. Probably, due to structural changes in the electrode (strong de-agglomeration and strong grinding), the conductive pathways (CB network) within the porous electrodes and the pore structure (increase in tortuosity) itself do not allow for fast ionic and/or electronic transport (increase in tortuosity) in the electrodes. The observations are in good agreement with the results obtained from morphology analysis of the electrodes (SEM) and the particle size distribution of the electrode pastes (PSA). Beyond this, the results on the twin-screw extruder are in alignment with previous studies on the influence of KC1 in batch-type processing [24,31]. Concluding the combined electrochemical studies, it occurs to us that the adaptation of the machine parameters, particularly KC1 during extrusion, considerably influences the final electrochemical performance of the electrodes and LIB cells, demonstrating the importance of process–product correlations and the impact of understanding and controlling the mixing process. However, by changing the process parameters, multiple effects (intended and unintended) occur in combination but to different extents, and process optimization needs to be completed by identifying a compromise between these effects. Based on our results, at KC1 = 60%, the de-agglomeration of carbon black is poorer, while the Gr particles are not influenced; however, at KC1 = 85%, where carbon black de-agglomeration occurs to a higher extent, the Gr particles are more strongly impacted through grinding. Using any KC1 within this range yields a combination of those effects accruing to different extents.

In this case, 70% KC1 yields the compromise for optimum cell performance, considering long-term and C-rate performance. At this point, CB is already de-agglomerated to a certain extent, while no substantial grinding of the Gr particles occurs, allowing optimized electron/ion conduction. At a high charge/discharge rate of 2C, 73.5% (102.1 mAh g⁻¹) of the initial capacity at C/10 (162.2 mAh g⁻¹) is achieved, demonstrating the high-power application of these cells.

4. Conclusions

The influence of kneading concentration 1 (KC1) as one of the most relevant process parameters of the extrusion process with regard to the properties of electrode pastes, electrodes, and final cell performance was investigated for graphitic active materials. Increasing KC1 initially results in a reduction in the electrode paste viscosity due to the higher energy input in the process. However, beyond a certain energy input threshold, independently of the graphite active material morphology, the viscosity rises again as KC1 is further increased, and the shape of the viscosity curve changes from linear to downward bent. Correspondingly, a change in the engine power from rising values for increasing KC1 to a decrease upon reaching the reversal point (corresponding to the process limit) was observed, indicating that this specific machine parameter indicates changes in the electrode paste. Further detailed analysis via SEM, PSA, and XRD revealed that particle grinding occurs beyond a certain KC1, which leads to a change in the surface structure of the graphite particles from hexagonal to rhombohedral. Nevertheless, this structural change does not influence the intercalation mechanism of graphite, while the increase in surface area due to grinding yields an increase in electrolyte decomposition and SEI growth. Consequently, lower first-cycle Coulombic efficiencies and reduced long-term charge/discharge cycling stability are accompanied by increasing KC1. In the case of C-rate performance, neither too low nor too high KC1 results in an optimum performance, suggesting that a medium KC1 yields an optimum compromise with respect to the two cell performance indicators. This optimum results from sufficient mixing and homogenization of the compounds of the electrode paste with a minor influence of particle grinding, sufficient but not excessive de-agglomeration of CB, yielding optimized structural properties of the electrodes with a proper electron conducting network, as well as sufficient tortuosity for enhanced ion transport channels. At too low KC1, though, de-agglomeration of carbon black is poor, and mixing and homogenization of the compounds are insufficient, while the Gr particles are not influenced by the shear forces. These effects result in the generation of a poor electron-conductive network, which in turn, is represented in a poor rate performance and the highest deviations in the obtained charge/discharge capacities of different cells. At too high KC1, on the other hand, carbon black de-agglomeration occurs to a high extent, and Gr particles are strongly impacted through grinding, yielding smaller particles and an increased surface area, which in turn, yields increased electrolyte decomposition and SEI formation and thus stronger degradation during long-term cycling, while the smaller Gr particles enhance Li-ion diffusion and yield an improved rate capability. In future works, advanced post-mortem analyses, including techniques such as TEM, Raman spectroscopy, and elemental mapping, can be applied to complement the structural observations and provide deeper insights into degradation mechanisms.

In addition, herein, it was found that machine parameters can be adduced for inline process development, which is virtually impossible with batch processes. For future new materials and recipes processed on an extruder, our results can help to directly identify unintended material destruction while optimizing the process by monitoring the machine parameters. In addition, our comprehensive results and correlations allow for rough estimates and predictions on how other materials behave within an extrusion process: Si/SiO_x and hard carbons used as active materials for sodium-based chemistries are probably more stable than Gr, indicating that structural changes in the bulk are unlikely. However, particularly hard carbons have micropores, suggesting that surface changes may occur during extrusion, indicating that lower KC1s might be favorable for processing these materials. Also, for cathode active materials that have a layered structure (e.g., NMC, LiCoO₂, and LiNiMnO₄) like graphite or even a highly stable olivine structure like LFP, a structural change is not to be expected as a result of the extrusion process, as the hardness is signifi-

cantly higher and may rather lead to the degradation of the screws. In these cases, high KC1s are likely beneficial for efficient homogenization.

Overall, unraveling, understanding, and exploiting process–product correlations during extrusion allows for specific tailoring of the properties of the electrode paste and thus the electrode and the final battery cell.

Supplementary Materials: The following supporting information can be downloaded at: <https://www.mdpi.com/article/10.3390/batteries11080299/s1>, Figure S1: Particle size distributions of the input materials Gr1, Gr2m, and CB. Figure S2: Shear rate-dependent viscosity of one electrode paste produced at different times (July/August/December of one year). Figure S3: Progression of the viscosities at specific shear rates (0.1 s^{-1} , 1 s^{-1} , and 1000 s^{-1}) depending on the kneading concentration 1 (KC). Figure S4: (a,b) Shear rate-dependent viscosity at different KC and (c,d) correlation of inverse viscosity and engine power for short and long kneading zones (solvent supply @ position 1 and 3, respectively). Figure S5: SEM images for electrodes prepared with 60% and 85% KC during the extrusion process. Figure S6: SEM images at several different spots for electrodes prepared with 60% and 85% KC during the extrusion process. Figure S7: Shear rate-dependent viscosity curves for (a) electrode pastes produced with and without CB at 70% and 85% KC and (b) electrode pastes produced with different amounts of CB and CMC. Figure S8: dQ/dV plot of Gr II Li cells utilizing Gr-based electrodes produced from electrode pastes with (a) 60% and (b) 85% KC1. Cells were cycled for 5 cycles at 0.05C discharge and 0.5C charge (these results belong to Figure 6 in the main manuscript. Table S1: Summary of the preliminary study (parameters that were varied and concrete parameter ranges that were set) performed by the authors to identify the most critical process parameter and for process optimization. Table S2: Results of the Rietveld refinement of the initial Gr material and samples prepared at different KCs during extrusion.

Author Contributions: Conceptualization, K.B. and M.B.; methodology, K.B., O.F., U.R. and M.B.; validation, K.B., O.F., U.R. and M.B.; formal analysis, K.B., M.B. and M.W.; investigation, K.B., O.F., U.R. and M.B.; writing—original draft preparation, K.B. and M.B.; writing—review and editing, M.W.; visualization, K.B.; supervision, M.W. All authors have read and agreed to the published version of the manuscript.

Funding: This research was funded by the German Federal Ministry of Education and Research (BMBF) “FoFeBat Teilprojekt1 and Teilprojekt2” (grants: 03XP0256, 03XP0416). Diffraction data were collected on a powder X-ray diffractometer funded by the Deutsche Forschungsgemeinschaft (DFG, German Research Foundation)—459785385.

Data Availability Statement: The original contributions presented in this study are included in the article/Supplementary Material. Further inquiries can be directed to the corresponding author.

Conflicts of Interest: The authors declare no conflicts of interest. The funders had no role in the design of the study; in the collection, analyses, or interpretation of data; in the writing of the manuscript; or in the decision to publish the results.

References

- Whittingham, M.S. History, Evolution, and Future Status of Energy Storage. *Proc. IEEE* **2012**, *100*, 1518–1534. [[CrossRef](#)]
- Manthiram, A.; Yu, X.; Wang, S. Lithium battery chemistries enabled by solid-state electrolytes. *Nat. Rev. Mater.* **2017**, *2*, 16103. [[CrossRef](#)]
- Balsara, N.P.; Newman, J. Comparing the Energy Content of Batteries, Fuels, and Materials. *J. Chem. Educ.* **2013**, *90*, 446–452. [[CrossRef](#)]
- Gielen, D.; Gorini, R.; Wagner, N.; Leme, R.; Gutierrez, L.; Prakash, G.; Asmelash, E.; Janeiro, L.; Gallina, G.; Vale, G.; et al. *Global Energy Transformation: A Roadmap to 2050 (2019 Edition)*; IRENA: Masdar City, United Arab Emirates, 2019.
- Liu, J.; Bao, Z.; Cui, Y.; Dufek, E.J.; Goodenough, J.B.; Khalifah, P.; Li, Q.; Liaw, B.Y.; Liu, P.; Manthiram, A.; et al. Pathways for practical high-energy long-cycling lithium metal batteries. *Nat. Energy* **2019**, *4*, 180–186. [[CrossRef](#)]
- Duffner, F.; Kronemeyer, N.; Tübke, J.; Leker, J.; Winter, M.; Schmuck, R. Post-lithium-ion battery cell production and its compatibility with lithium-ion cell production infrastructure. *Nat. Energy* **2021**, *6*, 123–134. [[CrossRef](#)]

7. Schmuck, R.; Wagner, R.; Hörpel, G.; Placke, T.; Winter, M. Performance and cost of materials for lithium-based rechargeable automotive batteries. *Nat. Energy* **2018**, *3*, 267–278. [[CrossRef](#)]
8. Haarmann, M.; Haselrieder, W.; Kwade, A. Extrusion-Based Processing of Cathodes: Influence of Solid Content on Suspension and Electrode Properties. *Energy Technol.* **2020**, *8*, 1801169. [[CrossRef](#)]
9. Haarmann, M.; Grießl, D.; Kwade, A. Continuous Processing of Cathode Slurry by Extrusion for Lithium-Ion Batteries. *Energy Technol.* **2021**, *9*, 2100250. [[CrossRef](#)]
10. Dreger, H.; Haselrieder, W.; Kwade, A. Influence of dispersing by extrusion and calendering on the performance of lithium-ion battery electrodes. *J. Energy Storage* **2019**, *21*, 231–240. [[CrossRef](#)]
11. Bockholt, H.; Indrikova, M.; Netz, A.; Golks, F.; Kwade, A. The interaction of consecutive process steps in the manufacturing of lithium-ion battery electrodes with regard to structural and electrochemical properties. *J. Power Sources* **2016**, *325*, 140–151. [[CrossRef](#)]
12. David, L.; Ruther, R.E.; Mohanty, D.; Meyer, H.M.; Sheng, Y.; Kalnaus, S.; Daniel, C.; Wood, D.L. Identifying degradation mechanisms in lithium-ion batteries with coating defects at the cathode. *Appl. Energy* **2018**, *231*, 446–455. [[CrossRef](#)]
13. Bauer, W.; Nötzel, D.; Wenzel, V.; Nirschl, H. Influence of dry mixing and distribution of conductive additives in cathodes for lithium ion batteries. *J. Power Sources* **2015**, *288*, 359–367. [[CrossRef](#)]
14. Dominko, R.; Gaberscek, M.; Drofenik, J.; Bele, M.; Pejovnik, S.; Jamnik, J. The role of carbon black distribution in cathodes for Li ion batteries. *J. Power Sources* **2003**, *119–121*, 770–773. [[CrossRef](#)]
15. Dreger, H.; Bockholt, H.; Haselrieder, W.; Kwade, A. Discontinuous and Continuous Processing of Low-Solvent Battery Slurries for Lithium Nickel Cobalt Manganese Oxide Electrodes. *J. Electron. Mater.* **2015**, *44*, 4434–4443. [[CrossRef](#)]
16. Li, J.; Fleetwood, J.; Hawley, W.B.; Kays, W. From Materials to Cell: State-of-the-Art and Prospective Technologies for Lithium-Ion Battery Electrode Processing. *Chem. Rev.* **2022**, *122*, 903–956. [[CrossRef](#)]
17. Wessel, J.; Turetskyy, A.; Cerdas, F.; Herrmann, C. Integrated Material-Energy-Quality Assessment for Lithium-ion Battery Cell Manufacturing. *Procedia CIRP* **2021**, *98*, 388–393. [[CrossRef](#)]
18. Bühler Group. Battery Trends: Why the Battery Industry is Embracing Continuous Mixing. Available online: <https://www.buhlergroup.com/global/de/stories/inspiration-hub/battery-trends.html> (accessed on 22 July 2025).
19. Kohlgrüber, K. *Der Gleichläufige Doppelschneckenextruder: Grundlagen, Technologie, Anwendungen*, 2., neu bearbeitete und erweiterte Auflage; Carl Hanser Verlag GmbH Co KG: München, Germany, 2016.
20. Seeba, J.; Reuber, S.; Heubner, C.; Müller-Köhn, A.; Wolter, M.; Michaelis, A. Extrusion-based fabrication of electrodes for high-energy Li-ion batteries. *Chem. Eng. J.* **2020**, *402*, 125551. [[CrossRef](#)]
21. Wiegmann, E.; Kwade, A.; Haselrieder, W. Solvent Reduced Extrusion-Based Anode Production Process Integrating Granulate Coating, Drying, and Calendering. *Energy Technol.* **2022**, *10*, 2200020. [[CrossRef](#)]
22. Bitsch, B.; Dittmann, J.; Schmitt, M.; Scharfer, P.; Schabel, W.; Willenbacher, N. A novel slurry concept for the fabrication of lithium-ion battery electrodes with beneficial properties. *J. Power Sources* **2014**, *265*, 81–90. [[CrossRef](#)]
23. Bitsch, B.; Willenbacher, N.; Wenzel, V.; Schmelzle, S.; Nirschl, H. Einflüsse der mechanischen Verfahrenstechnik auf die Herstellung von Elektroden für Lithium-Ionen-Batterien. *Chem. Ing. Tech.* **2015**, *87*, 466–474. [[CrossRef](#)]
24. Huber, K.; Adam, A.; Grießl, D.; Kwade, A. Understanding slurry mixing effects on the fast charging capability of lithium-ion battery cells: Methodology and case study. *J. Power Sources* **2022**, *536*, 231455. [[CrossRef](#)]
25. Metzger, T.G. *Das Rheologie Handbuch*: 5., Überarbeitete Auflage; Vincentz Network: Hanover, Germany, 2016.
26. Jeschull, F.; Brandell, D.; Wohlfahrt-Mehrens, M.; Memm, M. Water-Soluble Binders for Lithium-Ion Battery Graphite Electrodes: Slurry Rheology, Coating Adhesion, and Electrochemical Performance. *Energy Technol.* **2017**, *5*, 2108–2118. [[CrossRef](#)]
27. Ishii, M.; Nakamura, H. Influence of molecular weight and concentration of carboxymethyl cellulose on rheological properties of concentrated anode slurries for lithium-ion batteries. *JCIS Open* **2022**, *6*, 100048. [[CrossRef](#)]
28. Clasen, C.; Kulicke, W.-M. Determination of viscoelastic and rheo-optical material functions of water-soluble cellulose derivatives. *Prog. Polym. Sci.* **2001**, *26*, 1839–1919. [[CrossRef](#)]
29. Benchabane, A.; Bekkour, K. Rheological properties of carboxymethyl cellulose (CMC) solutions. *Colloid Polym. Sci.* **2008**, *286*, 1173–1180. [[CrossRef](#)]
30. TA Instruments. *Rheological Evaluation of Battery Slurries with Different Graphite Particle Size and Shape*; TA Instruments: New Castle, DE, USA, 2025.
31. Grießl, D.; Adam, A.; Huber, K.; Kwade, A. Effect of the Slurry Mixing Process on the Structural Properties of the Anode and the Resulting Fast-Charging Performance of the Lithium-Ion Battery Cell. *J. Electrochem. Soc.* **2022**, *169*, 20531. [[CrossRef](#)]
32. Inagaki, M.; Kang, F. Fundamental Science of Carbon Materials. In *Materials Science and Engineering of Carbon: Fundamentals*; Elsevier: Amsterdam, The Netherlands, 2014; pp. 17–217. ISBN 9780128008584.
33. Albetran, H.M. Structural Characterization of Graphite Nanoplatelets Synthesized from Graphite Flakes. 2020. Available online: <https://www.preprints.org/manuscript/202008.0325/v1> (accessed on 25 July 2025).

34. Huang, H.; Liu, W.; Huang, X.; Chen, L.; Kelder, E.M.; Schoonman, J. Effect of a rhombohedral phase on lithium intercalation capacity in graphite. *Solid State Ion.* **1998**, *110*, 173–178. [[CrossRef](#)]
35. Wen, B.; Zhao, J.J.; Li, T.J. Synthesis and crystal structure of n-diamond. *Internatia Mater. Rev.* **2007**, *52*, 131–151. [[CrossRef](#)]
36. Gallego, N.C.; Contescu, C.I.; Meyer, H.M.; Howe, J.Y.; Meisner, R.A.; Payzant, E.A.; Lance, M.J.; Yoon, S.Y.; Denlinger, M.; Wood, D.L. Advanced surface and microstructural characterization of natural graphite anodes for lithium ion batteries. *Carbon* **2014**, *72*, 393–401. [[CrossRef](#)]
37. Wakayama, H.; Mizuno, J.; Fukushima, Y.; Nagano, K.; Fukunaga, T.; Mizutani, U. Structural defects in mechanically ground graphite. *Carbon* **1999**, *37*, 947–952. [[CrossRef](#)]
38. Laves, F.; Baskin, Y. On the formation of the rhombohedral graphite modification. *Z. Für Krist.* **1956**, *107*, 337–356. [[CrossRef](#)]

Disclaimer/Publisher’s Note: The statements, opinions and data contained in all publications are solely those of the individual author(s) and contributor(s) and not of MDPI and/or the editor(s). MDPI and/or the editor(s) disclaim responsibility for any injury to people or property resulting from any ideas, methods, instructions or products referred to in the content.